GEM-based Dose Imaging Detectors for Proton Therapy Quality Assurance and Proton Radiography

Authors:

A.V. Klyachko

Affiliation:

Phenix Medical LLC,
Bloomington, IN, USA.

Correspondense address:

Email: *aklyachk@indiana.edu*

Abstract

Accurate, high-spatial resolution dosimetry in proton therapy is a time consuming task and may be challenging, due to the lack of adequate instrumentation. The paper describes the development of a novel dose imaging detectors based on gas electron multiplierz (GEM). Multiple needs are addressed in a single package by applying new detector technology to improve the speed, accuracy and cost-effectiveness of the quality assurance procedures.

A scintillation detector based on a double GEM amplification structure with optical readout was evaluated in pristine and modulated proton beams. The detector's performance was characterized in terms of linearity in dose rate, spatial resolution, short- and long-term stability and tissue-equivalence of response at different energies. Depth-dose profiles measured with the GEM detector in the 115 – 205 MeV energy range were compared with the profiles measured under similar conditions using the *PinPoint 3D* small-volume ion chamber. The GEM detector filled with a He-based gas mixture has a nearly tissue equivalent response in the proton beam and may become an attractive and efficient tool for high-resolution 2D and 3D dose imaging in proton dosimetry, in particular in small-field applications.

Scintillation GEM detector is also well suited for proton radiography applications, particularly in proposed efficient method for proton radiography-based QA of patient-specific devices based on the developed detector with the goal of improving accuracy, completeness and cost-effectiveness of the QA process in comparison with available alternatives.

1. Introduction

Presently, about 3% of the US population (~11 million people) are cancer survivors, a figure projected to grow to 18 million by 2022 [1]. More than a half of cancer patients are subjected to some form of radiation therapy during their treatment, and many of them suffer from the side effects, both short- and long-term. The dose from X-rays, conventionally used for radiation therapy, shows exponentially decaying energy deposition in tissue with increasing depth beyond a build-up region, damaging the normal tissue both ahead of and behind the tumor and thus may cause both short-term toxicity and later stage tumors in long-term cancer survivors. Nowadays, as an alternative, the patients increasingly have access to relatively new treatment modality, the proton therapy. In contrast to photons, protons show increasing energy deposition with penetration depth, with maximum energy deposition near the end of the range of the proton beam (Bragg peak). The region of maximum energy deposition can be positioned within the tumor, creating a very conformal high dose region. The dose region created by a spread-out Bragg peak (SOBP), the sum of appropriately weighted several individual Bragg peaks with varying incident proton energies, can cover the entire tumor volume with high accuracy, whereas the doses to healthy tissue are lower than during conventional photon therapy, see Fig. 1 (the figure is adopted from [2]).

Although advances in X-ray therapy techniques, such as introduction of intensity-modulated photon therapy and volumetric arc therapies, now allow to deliver almost as highly conformal and uniform dose to a tumor as with protons, the relative advantage of proton therapy in sparing normal tissues has never been more apparent or important [3]. Proton therapy minimizes side effects and treatment-related morbidity, including secondary cancers, cardiovascular disease, fertility complications, and other late effects, resulting in a better quality of life for the patients in comparison with photon radiation therapy. It also allows to carry out the treatments of tumors located adjacent to critical organs, such as brain and spine, which can't be done using photons. Avoiding even moderate doses to these vital organs is impossible with X-ray radiation therapy.

In recent years, the number of proton therapy facilities worldwide has been rapidly growing. A recent projection [4] predicts that the number of proton therapy rooms treating patients on a regular basis will triple by 2019, and will increase by an order of magnitude by 2030, with 1,200 to 1,800 proton therapy rooms available to patients worldwide, from the 110 rooms available in 2012 (the number was 8 in 1990).

The number of cancer patients affected by the development is likely to increase at an even greater rate, as proton therapy becomes more widely applied and technological improvements enhance patient throughput. In 2013, the ten operational proton therapy centers in the U.S. treated a total of about 7500 patients per year. That accounts for less than 1% of all patients who receive radiation therapy, while at least 30% of patients who receive radiation therapy would benefit substantially from the use of protons with current protocols [5]. It is reasonable to assume that with the new generation of technical improvements, the number of proton therapy patients will increase by an order of magnitude within a decade. Yet, proton therapy remains relatively little-known among the general public and even practicing doctors and medical physicists. Increasing awareness of this superior cancer treatment modality among the general physics audience is one of the aims of this article.
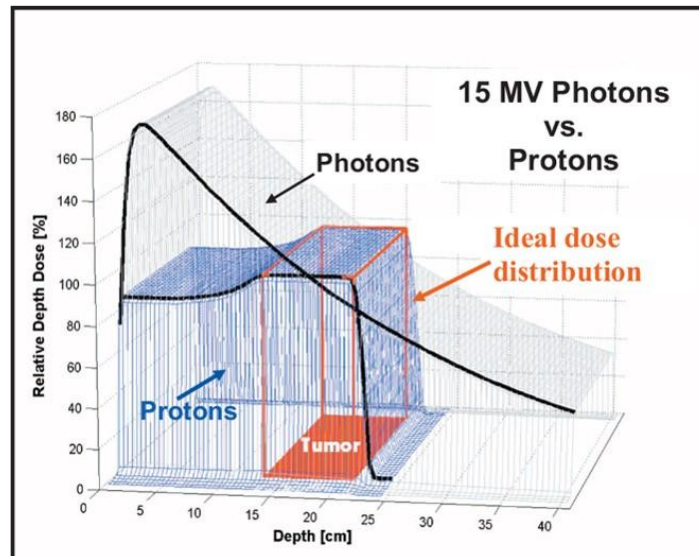
Figure 1. Comparison between the depth dose curves for 15 MV photons and a proton spread-out-Bragg peak (SOBP). A target volume is shown in red. Shown also in red lines is an "ideal dose distribution" for the target volume, which provides uniform, maximum dose to the target volume and zero dose outside the target volume.
The proton dose distribution approaches the ideal case to a much greater extent than does the photon dose distribution. Notably, the proton dose stops abruptly distal to the target volume and delivers less dose to the region proximal to the target volume.

Treatment with protons requires a high level of quality control and quality assurance (QA) in order to gain a real clinical benefit from the physical and radiobiological advantages of protons. Basically, the same reasons which make protons so useful for radiotherapy applications (*i.e.* the finite range and the steep fall-off in dose deposition after the dose maximum) are also the reasons why a very good conformance between planned and delivered dose is critical. With photon radiotherapy one can safely assume that the dose distribution would cover the whole longitudinal extent of a tumor and beyond. In case of protons this assumption does not hold anymore: the Bragg peak can cause major problems if applied improperly; an excessive damage to healthy tissues can occur or even parts of the tumor can be left untreated if there are significant differences between planned and delivered dose. Therefore, patient-specific quality assurance pre-treatment verification programs are implemented to achieve a high

spatial and dosimetric accuracy during the treatment delivery.

In recent years, active methods of beam delivery, where the tumor is "painted" in all three dimensions by scanning a narrow (pencil) beam with variable energy, have been developed to improve the conformance of proton therapy. While the versatility of such systems is attractive, they present challenges for dose delivery verification. Implementing scanned proton beams for cancer treatment has generated the need for a new class of QA systems that permit rapid and accurate two- and three-dimensional data acquisition. QA systems for scanned proton beams must also be adaptable to the timing structure and energy stacking of treatment delivery. In many cases, it is also necessary to accurately characterize the intensity distribution within a single pencil beam to provide adequate input data for the configuration of the treatment planning system. Additional requirements on sensitivity and dynamic range of the

measuring system are imposed by the need for accurate measurements for both high- and low-dose envelopes of single pencil beams.

Existing detectors for 2D dose distribution measurements such as gafchromic films [6], scintillating screens [7, 8] and gels [9] have been used in proton beams with varying degrees of success. While having sufficiently high, sub-millimeter spatial resolution, the response of these detectors to absorbed dose is non-linear. Accurate dose reconstruction is further complicated by various quenching effects, resulting in a non-linear dose response as a function of beam energy. In addition, film and MRI gel detectors require long signal processing time of the order of minutes or hours. Also, the dynamic range (signal-to-noise ratio) of the commercially available scintillation screen detector LYNX [8] and Gafchromic EBT films [6] is $\sim 10^2$, not adequate to characterize the pencil beam profile accurately enough [10]. Characterization of the spot "halo", the broad profile tails containing a substantial fraction of the delivered dose, requires a dynamic range of $\sim 10^4$ [11].

Ion chamber arrays are free of those shortcomings and have been successfully used for verification of dose distributions and quality assurance in proton therapy [12, 13]. However, with spatial resolution of several millimeters, these devices are not well suited for obtaining accurate dose distributions in radiation fields characterized by high dose gradients. Furthermore, many ion chambers provide two independent one-dimensional measurements of dose distributions, without sensitivity to possible 2-D correlations that can distort a pencil profile. Improvement in spatial resolution of such detectors is challenging: due to the lack of charge amplification, the signals from such detectors become very small with decreasing pixel size. They require complicated and rather expensive custom electronics to achieve acceptable signal-to-noise ratio, which limits the number of channels and therefore the position resolution and/or area coverage that these detectors can provide.

These problems can be solved by the implementation of gaseous amplification devices, such as Gas Electron Multipliers (GEMs). GEMs were first introduced by F. Sauli two decades ago [14] and mostly used as tracking detectors in high-energy physics experiments. They offer fast performance, high sensitivity and spatial resolution, robustness and flexibility in the detector design, allowing for both electronic and optical readout schemes, and the option to cascade GEMs in order to improve the signal to noise ratio. The principles of GEM operation are outlined below. Although GEMs mainly have been used as gaseous preamplifier devices with electronic readout, it has been shown that, when suitable gaseous mixtures are used, a large number of photons are emitted as electrons in GEM interact with gas molecules [15, 16]. These photons can be utilized to create an image of a proton beam. Soon after the introduction of GEM, this scintillation, read out by a CCD camera, has been utilized in the design of an imaging detector [17]. First results on the development of 2D dose imaging detector prototypes with optical readout were reported in [18-20].

Detectors based on GEMs are promising candidates for dosimetry systems of two kinds. One system, with electronic two-dimensional readout [21], would be a fast (microsecond timing resolution), moderate spatial resolution (~1-2 mm, limited by the cost of electronics) dose imaging detector for online monitoring of scanning beams. Such detector, with cross-strip readout, would also be a good candidate for low-rate applications, such as proton tomography. Another detector system, with optical readout [18-21], would be a slower, moderately priced detector with

sub-millimeter spatial resolution suitable for dose distribution verification and quality assurance measurements in hadron therapy. Development of a GEM-based detector system with electronic readout has been reported elsewhere [21]. Here, we will concentrate on GEM-based dose imaging detectors with optical readout.

One of the promising applications of GEM detectors is proton radiography. Since spatial response variations in a GEM detector are associated with particular GEM foils, they can be corrected by applying a pixel-by-pixel correction matrix derived from an image obtained by illuminating the whole detector working area with a uniform proton field. Analysis of images of heterogeneous objects and consecutive beam deliveries indicate the ability to detect dose variations on the level of <1%, far surpassing radiochromic films in sensitivity and operability.

One of the proton radiography applications of the scintillating GEM detector is aimed at dose delivery systems that employ passive scattering and uniform scanning (and in some cases pencil beam scanning systems), which utilize complex patient-specific devices (PSDs) such as those in Fig. 2 to make the delivered dose conform as closely as possible to the tumor volume. The field is constrained laterally to the maximum extent of the target volume by a metal alloy collimator thick enough to stop the unwanted portions of the beam. A range compensator (RC) made from low-Z material is used to correct the protons' range distribution for patient surface irregularities, density heterogeneities in the beam path, and changes in the shape of the distal target volume surface. The shape of the isodose surface at the distal edge of the beam is modulated by controlling the RC's depths, so it is very sensitive to changes of the shape, size, and depth of the RC – a change in the RC thickness of 1 mm, for example, results in 1.1-1.2 mm (depending on the RC

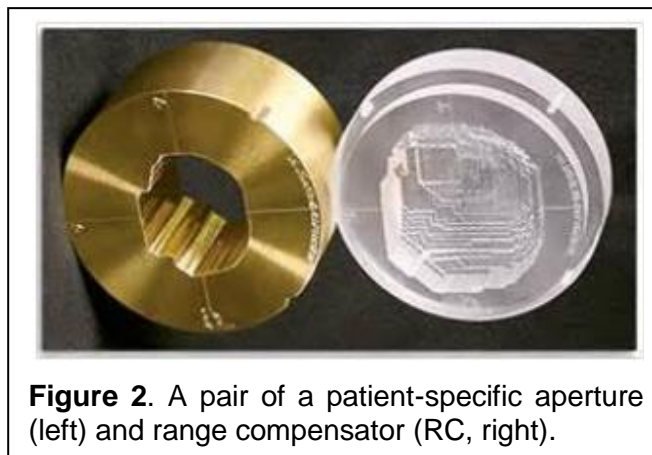material) displacement of the beam distal edge in the patient for the affected voxels.

Figure 2. A pair of a patient-specific aperture (left) and range compensator (RC, right).

Inaccuracies in machining of PSDs compromise the dose conformity and target coverage since physical defects created during the manufacturing process can lead to errors in the field range and shape. Thus, QA testing of aperture and compensator over the entire exposed region of the RC is critically important for accurate delivery of the planned dose. Conventionally, patient-specific devices are manufactured using CNC milling machines [22] according to the geometry calculated by the treatment planning system. A computer-controlled endmill is used to mill the inside of a cylindrical or rectangular blank made of Lucite or wax of standardized shape and uniform density. Several errors can occur during the CNC manufacturing process. In particular, depth differences (DDs) caused by limitations in the size or tapering angle of the endmill can extend over the entire RC, and these errors must be fully characterized by precision QA.

Traditionally, fabricated PSDs are manually inspected to confirm that the collimator's shape and RC's thickness match the plan ones within the specified tolerance (typically <1 mm [23]), by carrying out the measurements at sampled points with a manual depth gauge or a touch-sensor depth measurement system [24]. These methods, however, are of only limited effectiveness,

due to the limited number of examined verification points together with the difficulty of point matching a manufactured PSD with a planned one. Specifically, since an actual RC is manufactured using a tapered endmill of a given tip diameter and taper angle, overall shifts take place from the center of a matrix toward the radial direction, narrowing the comparable region between them and causing sizable thickness differences (TDs), especially in a large gradient region. This is also a labor- and time consuming task: quality assurance measurements on a patient-specific RC can take anywhere from 10-15 minutes (for a relatively small field) to several hours, while measuring the depths of only a small fraction of milled points.

Some studies have attempted to develop automated QA methods. A planar x-ray image-based QA technique employed in [25] could provide whole volume information and analyze the depth differences. However, this technique required extensive image processing to minimize random, line pattern, and background noise as well as blurring of the image due to x-ray scattering. The study [26] developed an automatic QA method based on computed tomography (CT), which requires the use of a marker or the application of a threshold value on the CT images to determine a reference thickness. As a result, a part of the RC geometry could be lost owing to the finite slice thickness of the CT scan. Both these radiation image-based approaches have their limitations and are time consuming. An optical 3D scanning-based automatic QA system for proton range compensators has been developed [27] . The system proved to be efficient, although RC QA time was still about 20 min on average. Also, optical camera-based 3D systems are known to exhibit errors when obtaining surface data from regions of greater depths and abrupt thickness changes.

The feasibility of proton radiography with radiochromic film as an RC QA tool was investigated [28, 29]. In order to obtain a radiographic RC image in a single film, Gafchromic EBT3 films were exposed through RCs with a proton beam. The currents of individual Bragg peaks in a spread-out Bragg peak (SOBP) were modulated with weighting factors in such a way that the depth-dose characteristic of the resulting field was similar to that of photon beams, maximizing the linearity of optical-density-to-thickness ratio. The optical densities of the EBT film were digitized to pixel values and then converted to thickness using a thickness-pixel value calibration curve. The thickness information on the radiographic image was compared with plan data that had been extracted from the treatment planning system. The QA results demonstrated the potential utility and clinical applicability of the proton radiography based QA method.

Radiochromic film, though, is not an ideal medium for high resolution proton radiography. While having sufficiently high, sub-millimeter spatial resolution, the response to absorbed dose is non-linear as a function of dose and beam energy. It is not a real time detector; irradiation, development and digitization of a film is time consuming. More importantly, a ~3% intrinsic non-uniformity of response across the film [30] significantly limits the sensitometric resolution of a method relying on a film. Scanning a film twice, before and after exposure, so that the unexposed film image could be subtracted from the exposed film image as was done in [28], can help correct for non-uniformity of the optical density of the film, but not for intrinsic non-uniformity of film sensitivity to radiation. A full-scale scintillation GEM detector would far surpass radiochromic film as a proton radiography tool.

In this paper, we describe the development of scintillation Gas Electron

Multiplier (GEM) detectors that meet the QA demands for both proton beam characterization and accurate PSD measurements. The aim of the studies described here is thus two-fold: (i) – develop a full-scale detector for acquiring a fast and accurate 2D image of the dose distribution, suitable for use in clinical proton beams for pre-treatment patient-specific dose verification, machine QA and beam commissioning, significantly surpassing currently available detectors in sensitivity and position resolution, combined with high linearity of response and data acquisition speed; and (ii) – develop a proton radiography technique and an efficient automated method for proton radiography-based QA of patient-specific devices based on the developed detector.

2. Materials and Methods

The principles of GEM operation have been described in [14,31] and are only briefly outlined here. A GEM consists of a set of holes arranged in a hexagonal pattern (typically 70 μm diameter at 140 μm pitch), etched through a copper–kapton–copper thin-foil composite, as shown in Fig. 3a. Application of an electric potential between the two sides of the GEM generates an intense electric field (Fig 3.b, [31]). Electrons released by the ionization in the gas outside of a GEM drift into the holes and multiply in the high electric field.

A unique property of GEMs, as compared to other micro-pattern detectors, is their capability to operate in cascade, i.e. in a multi-GEM structure. Sharing the avalanche multiplication among several cascaded electrodes allows operating GEM detectors at high overall gains in the presence of highly ionizing particles, while decreasing the probability of hazardous discharges.

The design of the GEM detector is schematically shown in Fig. 4. The primary beam ionizes gas molecules in the detector's sensitive volume creating electrons which drift in the electric field toward the GEMs and undergo gas multiplication in the GEM holes. The light emitted by the molecules of a scintillating gas mixture excited during the electron multiplication is reflected into a CCD camera lens by a mirror. The light intensity is proportional to the number of secondary electrons [18], hence the light intensity distribution read out by the CCD camera is expected to be proportional to the 2D dose distribution deposited by the primary beam. The image is truly two-dimensional, in contrast to conceivable tracking detectors that could provide two successive 1D measurements which lack correlations affecting beam shape.
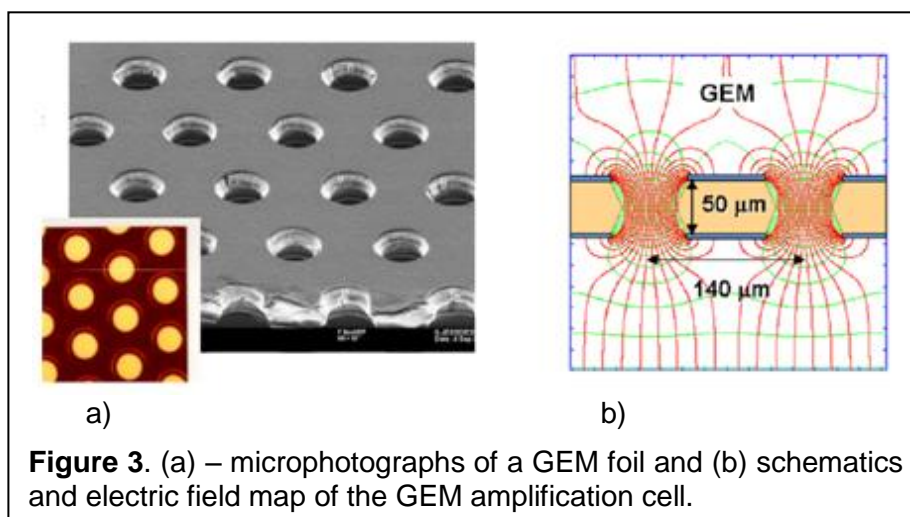

Figure 3. (a) – microphotographs of a GEM foil and (b) schematics and electric field map of the GEM amplification cell.
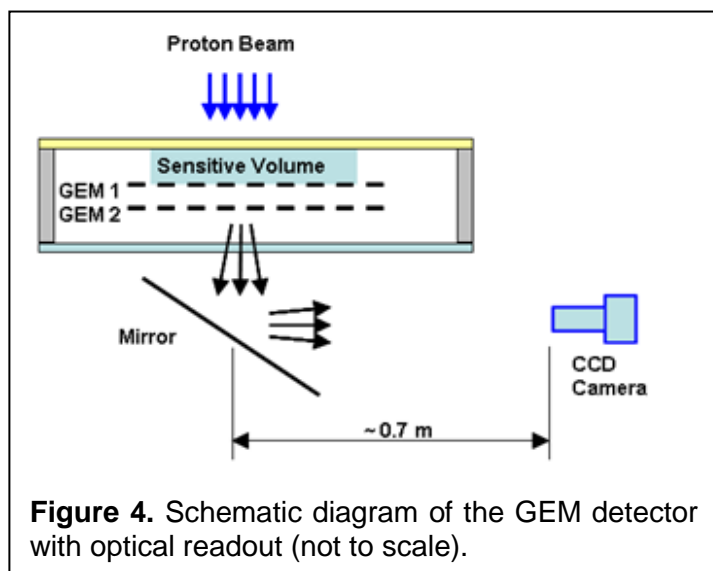
Figure 4. Schematic diagram of the GEM detector with optical readout (not to scale).

The last GEM 2 surface is kept at ground potential, while the rest of GEM surfaces and cathode are biased using individual negative polarity power supplies. The voltages are set to maintain the drift field in the sensitive volume at about 1.5 kV/cm and transfer field between the GEMs at about 1.7 kV/cm, and across GEMs in the 200 – 400 V range depending on the intended application mode. The sensitivity of the detector is proportional to the voltages across the GEM foils; the higher the sensitivity, the lower is the dose rate limit of linear operation mode. Over the years, a number of GEM detectors were designed and tested, a 10x10 cm^2 detector characterized in [32] and a full-size 28x28 cm^2 OptiGEM detector [33] shown in Fig. 5, among them. While this design generally follows that of the first double-GEM prototypes described in [21, 34], a number of important changes were made in order to improve the detector performance. In particular, low-outgassing Rexolite entrance windows were introduced, with the size sufficient to utilize all of the sensitive area of the GEM foils used (10x10 cm^2 GEM foils with double-conical holes (50 μm inner diameter, 140 μm pitch) manufactured by Tech-Etch [35] and 28x28 cm^2 foils with similar geometry from CERN workshop). The cathode was mounted directly on the

inner side of the entrance window, eliminating the space between the window and the cathode. A CCD camera Model QSI RS 3.2 by Quantum Scientific Imaging [36] with thermoelectric cooling, featuring a higher-resolution sensor and having spectral sensitivity better matching the emission spectrum of the gas mixture was used. The CCD's pixel size translates to effective pixel size at the anode (GEM 2) measurement plane of 0.0895 mm^2 in 10x10 cm^2 detector and 0.205 mm in OptiGEM, in each of two dimensions. Better quality lenses were utilized and overall improvements were made to light sealing of the detector housing. The inner surfaces of the detector housings were anodized or painted black in order to reduce the amount of reflected light reaching the CCD sensor. Layers of lead and borated polyethylene were added around the CCD camera in order to shield the CCD sensor from secondary particles.
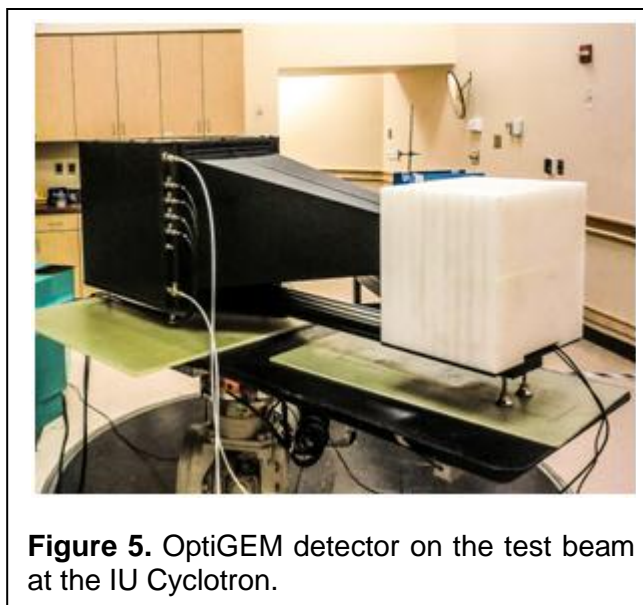

Figure 5. OptiGEM detector on the test beam at the IU Cyclotron.

The GEM detector's response to proton radiation depends on the properties of the gas mixture filling its sensitive volume. The choice of gas mixtures for scintillation GEM detectors is discussed in detail in [32]. Air-filled ion chambers are successful as water-equivalent dosimeters in proton beams due to the constancy of the air-to-water mass stopping power ratio: it varies less than 0.5%

as a function of beam energy over the clinical proton therapy range from about 230 MeV down to about 20 MeV in the Bragg peak region. However, air produces neither sufficient gas amplification nor substantial light output when exposed to protons of clinical energies. Therefore one must find a scintillating gas mixture with mass stopping power properties similar to that of water. Amongst a number of scintillating mixtures used in gas detectors, combinations of Ar or He with CF_4 attracted the most attention due to their considerable light emission in wavelength regions (300 – 1000 nm) well matched to the spectral response of CCD cameras [37]. At proton energies ~20 MeV characteristic for the Bragg peak, Ar-based mixtures have relative stopping power values somewhat lower than that of air. For He-based mixtures, the proportion of He and CF_4 can be chosen such that the stopping power of the mixture remains within ~1% of that for air for proton energies above 20 MeV. In particular, a 60/40% He/CF_4 mixture is a good candidate for the GEM detector, allowing for more accurate characterization of the Bragg peak compared with the Ar/CF_4 (95/5%) mixture used early on (for example [20, 34]). The light yield of He-based mixtures is several times lower than that of Ar-based ones, but is still sufficient for most dose imaging applications.

During operation, the detector is continuously flushed with gas mixture at 1 atm. The gas flow of ≈2 l/h has to be started >12 h in advance to allow the flowing of multiple detector volumes of gas through the detector's sensitive area before the start of measurements. We used either the Ar/CF_4 (95/5%) or the He/CF_4 (60/40%) gas mixture, each provided pre-mixed in a pressurized bottle. The choice of two gas mixtures instead of just one (He/CF_4) was driven by the application, gas mixture availability and cost considerations (He-based mixture is significantly more expensive).

Testing and characterization of GEM detectors was performed at the Indiana University Cyclotron, first in a static quasi-continuous 205 MeV proton beam of the Proton Dose Test Facility (PDTF) and later in a uniform scanning beam delivery system [38] of the Indiana University Health Proton Therapy Center (IUHPTC). The scanning system delivers the beam of a constant intensity, deflecting it in the horizontal and vertical directions and providing laterally uniform dose coverage of the prescribed area. The scanning process is repeated at a rate of about 14 Hz until the prescribed dose at the given depth is reached. Beam energy control is provided through the use of a binary slab range modulator to create a spread-out Bragg peak (SOBP). The final shaping of radiation fields in the transverse direction is achieved by brass apertures.

For the duration of the GEM evaluations spanning a number of years, an Advanced Markus (Model 34045) ion chamber by PTW [39] having absolute dose calibrations traceable to NIST was used for periodic absolute dose calibrations of the beam delivery system. This information served as reference for ensuring consistency of measurements across individual dose delivery sessions. The GEM signal was converted to dose after cross-calibrating it against a Markus or PinPoint 3D (Model 31016) ion chamber by PTW, also with absolute dose calibrations traceable to NIST. The PinPoint chamber was also used as a reference detector in the measurements of depth-dose distributions.

Detailed description of experimental setups used for obtaining depth-dose and transverse distributions, as well as procedures of data acquisition, background subtraction and data analysis can be found in [32, 34].
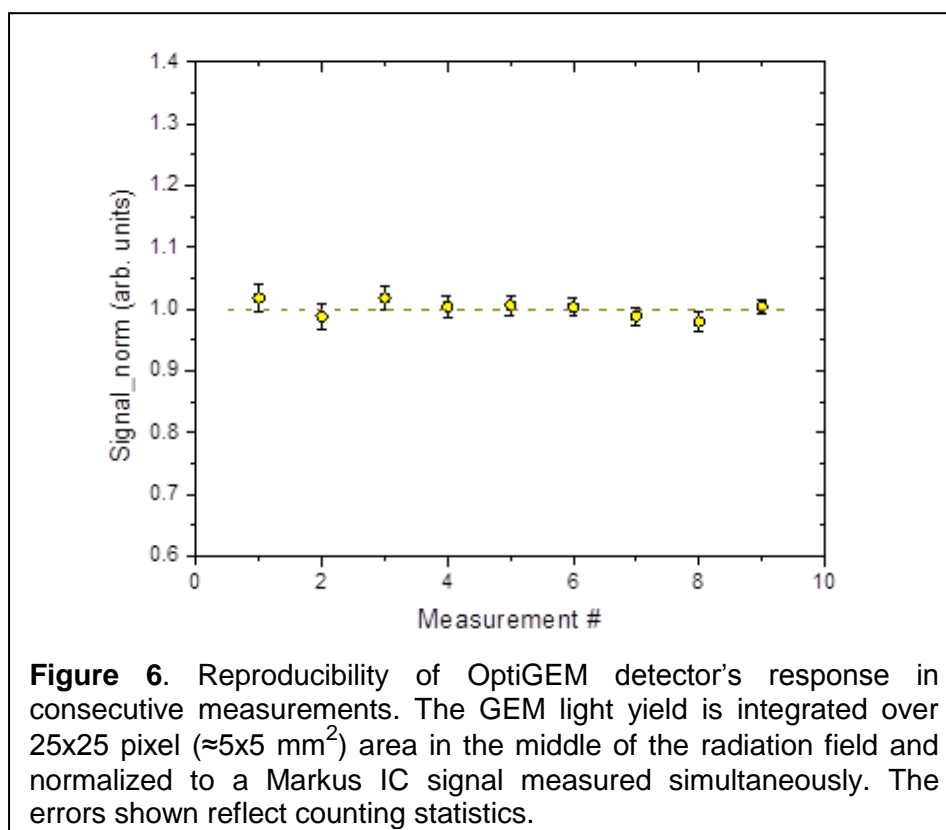
3. Results and Discussion

Due to space limitations, only a fraction of results is presented here. More

comprehensive data obtained with the 10x10 cm^2 detector can be found in [21, 32, 34]

In the initial start-up (starting irradiation after a long period of inactivity), the detector response decreases by several percent as more dose is delivered. This behavior is attributed to a charging effect known to be characteristic of GEM detectors in general. The detector response stabilizes after irradiating the detector with a proton dose of 3-5 Gy. In subsequent measurements during the day, the signals from individual pixels fluctuate typically within ±1-2%, while the detector response remains stable overall. The reproducibility of the detector response after start-up is shown in Fig. 6.

The unprocessed dose images obtained with the detectors may exhibit considerable response variations with position within the active area. These variations arise from gain variations due to differences in GEM foil hole diameters and shapes and/or in sensitive detector region thickness across the active area, as well as pixel-to-pixel gain variations in the CCD camera sensor and the effects of optical obstructions (vignetting and dust). Throughout the period of a day, the relative pixel-to-pixel signal in multiple measurements for reproduced delivered doses has been demonstrated to remain constant within ±2%. Since the spatial response variations are associated with particular GEM foil features in the detector and particular camera pixels, they can be corrected by applying a pixel-by-pixel correction matrix to the acquired images. Such a matrix can be derived from an image obtained by illuminating the whole detector working area with a uniform proton dose field. An image of a 10x10 cm^2 flat proton field obtained with OptiGEM detector and transverse profiles before and after correction are shown in Fig.7. Note that the ripple on the vertical profile flattop reflects the field non-uniformity due to beam wobbling. After corrections, the spatial response non-uniformity is <±2%.

Figure 6. Reproducibility of OptiGEM detector's response in consecutive measurements. The GEM light yield is integrated over 25x25 pixel (≈5x5 mm^2) area in the middle of the radiation field and normalized to a Markus IC signal measured simultaneously. The errors shown reflect counting statistics.
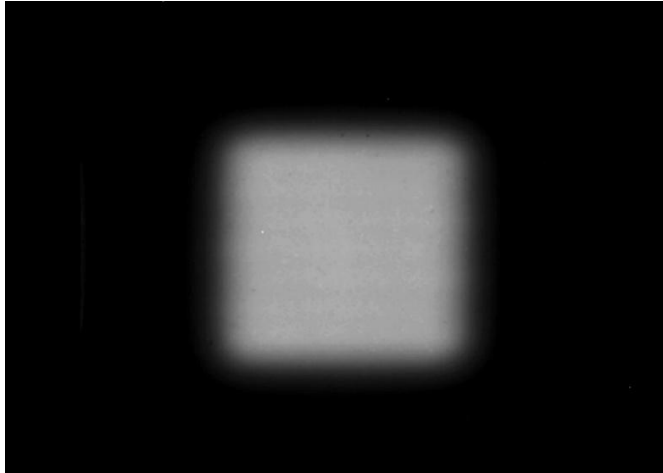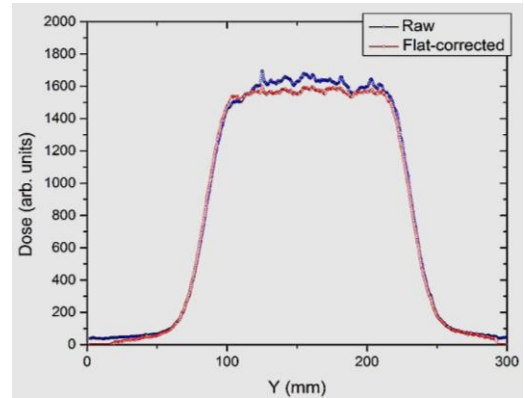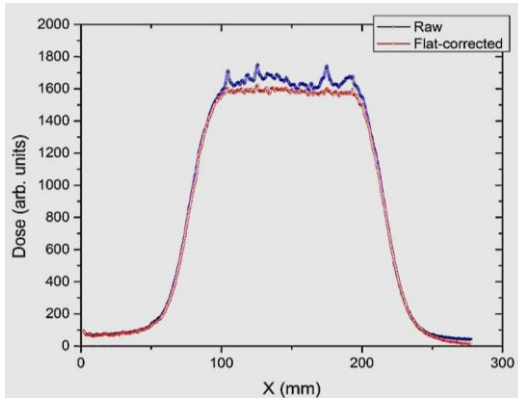
Figure 7. Top: image of a 10×10 cm^2 proton field. Bottom: horizontal (left) and vertical (right) field profiles along 10-pixel (2 mm) wide bands in the orthogonal directions, before (blue) and after (red) the flat-field correction for response non-uniformity.

The spatial resolution of the 10x10 cm^2 GEM detector was estimated by comparing dose profiles obtained with the GEM detector and EBT2 film imaging a narrow 0.95 mm slit in identical conditions, see Fig. 8 [32]. For ease of comparison, the profiles are normalized at their respective maxima. The spatial resolution in the measured film profiles is chiefly determined by the scanner resolution, which was set to be similar to that of the GEM detector's effective pixel size. As can be seen in Fig. 8 the full width at half maximum (FWHM) values measured with the GEM detector and film are generally in good agreement. The slit profiles are fitted with a superposition of two Gaussians: the primary curve characterizes the detector response while the secondary, broader Gaussian represents protons scattered from the collimator walls and, in the case of GEM detector, also light reflections inside the detector. FWHM values of primary Gaussians in the slit images for the GEM detector and film are 1.17 and 0.93 mm, respectively, and therefore the width of GEM detector's Gaussian line spread function can be estimated as FWHM = 0.68 mm (σ=0.29 mm). A slit image obtained with the OptiGEM detector is shown in Fig.9. The main peak is fitted with Gaussian curve with FWHM of 1.6 mm. The width of the line spread function of the detector itself can be estimated, taking into account the width of the slit, as FWHM = 1.3 mm (σ=0.53 mm).

In both Figs. 8 and 9, the GEM response shows a systematic broadening in the low isodose tails, which is attributed to light scattering inside the GEM detector, including the copper GEM foils, mounting frames, and housing. The relatively close placement of the 45 degree mirror to the detector's exit window may also contribute to the unwanted light reflections.
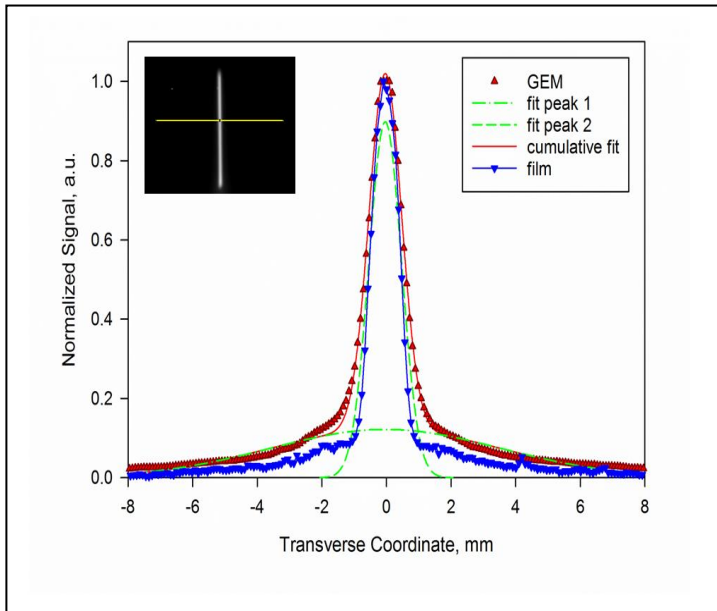
Figure 8. Transverse light intensity profiles across images of a 0.95-mm wide slit recorded by the 10 cm GEM detector red curve) and EBT2 film (blue curve) in identical irradiation conditions. The inset shows the GEM image and the 3-pixel (0.3 mm) wide band along which the profile was plotted.
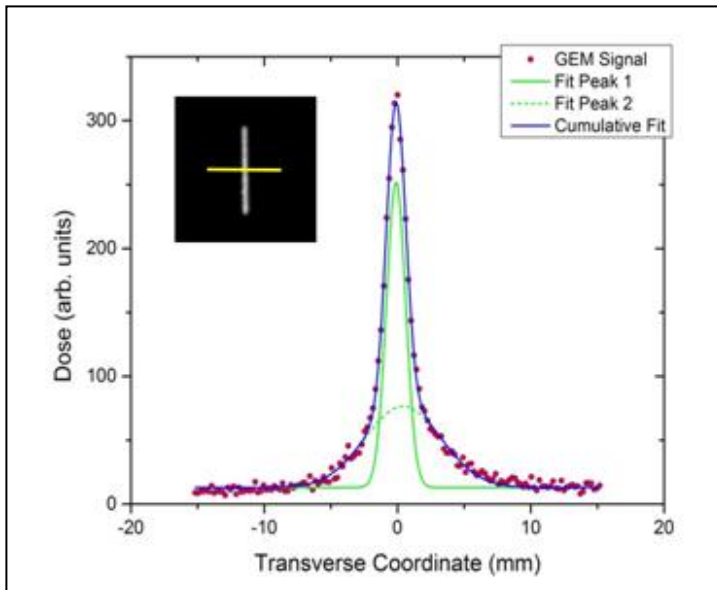

Figure 9. OptiGEM Image of the 1.0 mm slit collimator (inset) and light intensity profile along a 5-pixel-wide (1 mm) band indicated in the image, and corresponding fit with a superposition of two Gaussians.

The GEM detector response as a function of beam intensity (average dose rate) in Fig.10 shows good proportionality between the beam intensity and the detector's optical output in the whole range of the dose rates studied [32]. The range of beam currents used for this study corresponds to the typical average dose rates used in patient treatments under the uniform scanning beam delivery technique. Although average dose rates at the detector location during these tests were between 50 and 450 cGy/min, it should be noted that, due to the scanned nature of the beam delivery, instantaneous dose rates were much higher, in the $7 - 60$ Gy/min range. (During the 10 cm detector testing with the Ar/CF_4 gas mixture in a static beam, the detector demonstrated a linear response up to dose rates of 70 Gy/min).
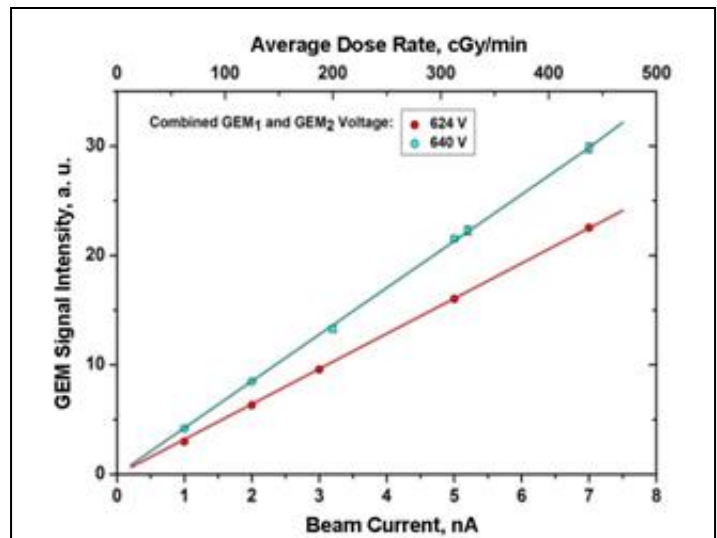

Figure 10. The GEM detector response (10 cm detector with He/CF4 mixture) as a function of beam current, at two GEM bias settings. The average dose rate (upper scale) at a given beam current is estimated from measurements with an ion chamber in similar geometric conditions. Experimental error bars, where not shown, are smaller than the point size.
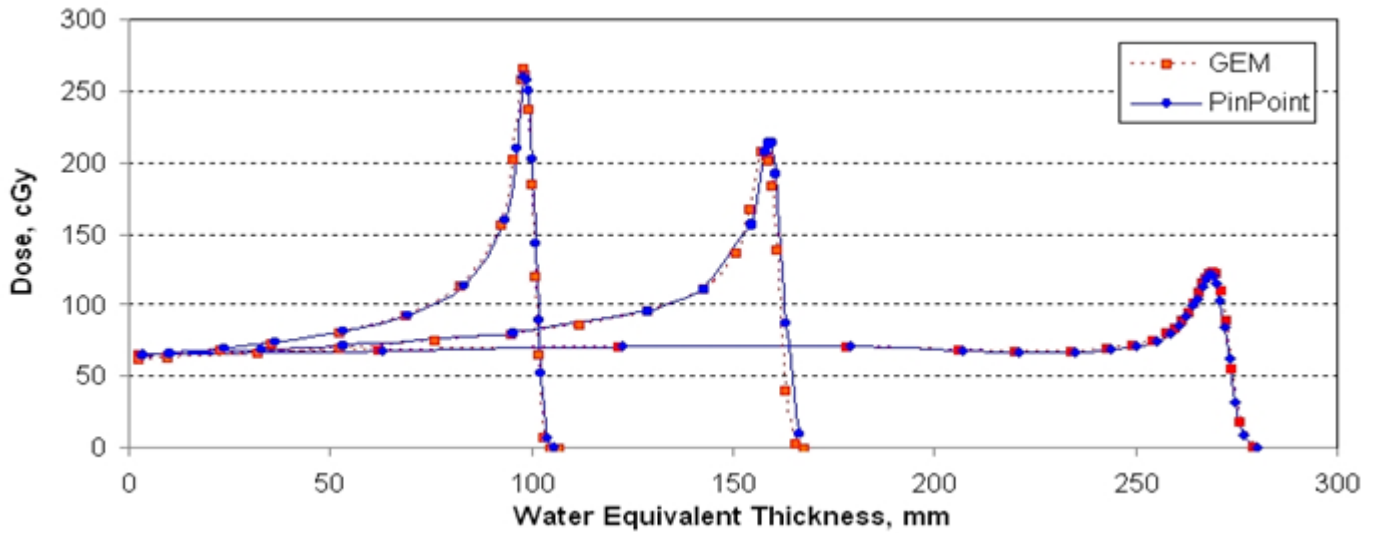
Figure 11. Depth dose profiles on the beam central axis for pristine beams with 10, 16 and 27 cm range in water collimated by a 1 cm diameter aperture, measured with the 10cm GEM detector with He/CF$_4$ gas and the PinPoint ion chamber in an acrylic phantom. Experimental error bars are smaller than the data points.

Figures 11 and 12 illustrate the excellent agreement between depth dose distributions measured with the GEM detector and with the PinPoint chamber [32]. The results are compared in Fig. 11 for pristine beams with 10, 16 and 27 cm range in water, and in Fig. 12 for a modulated beam with 4.8 cm SOBP extent. Measurements for other ranges in water and with other aperture diameters demonstrated similarly good agreement between the GEM detector and PinPoint. The observed good agreement with the PinPoint chamber suggests that the GEM detector with the He/CF$_4$ gas mixture can become a good alternative to a small volume ion chamber in depth dose and lateral profile measurements. A unique property of the GEM detector is its ability to simultaneously provide excellent (sub-millimeter) spatial resolution on the absorbed dose profile and information integrated over the detector's sensitive volume. The measured dynamic range of the prototype detector (mostly determined by the CCD camera's signal-to-noise ratio of 77 dB) was $6 \cdot 10^3$: 1, making it a good candidate for accurate pencil beam profile measurements.

Examples of proton radiographic images obtained with the 10 cm GEM detector are shown in Fig. 13. The objects were positioned at the face of the GEM detector and irradiated with ~100 cGy dose in the 153 MeV pristine proton field. The images are corrected for field and detector response non-uniformities. These images demonstrate high spatial resolution and high sensitivity of the technique.
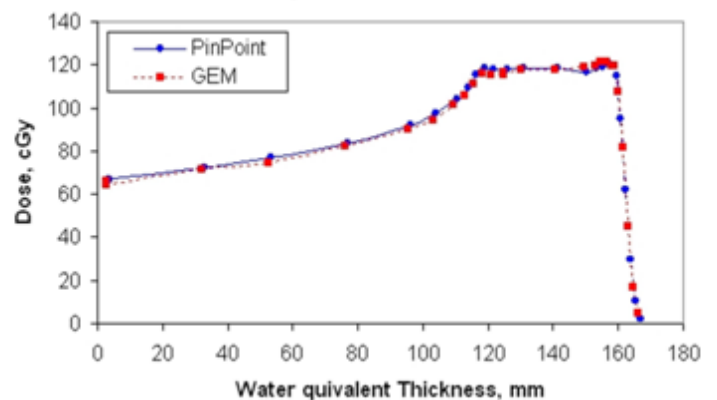

Figure 12. Central axis depth dose profiles of a modulated beam with a 5-cm SOBP extent and 16-cm penetration range in water, measured in the acrylic phantom with the GEM detector and the PinPoint ion chamber for aperture diameter 2 cm. Error bars are smaller than data points.

However, a pristine (unmodulated) beam used to obtain these images, in combination with integrating imaging detector, is not sufficient to accurately assess the thickness of the objects. Two different proton radiography methods sensitive to object thickness have been proposed: a) tracking each proton traversing the object and measuring its remaining energy [40, 41], and b) modulating the proton beam range to produce a depth–dose distribution similar to that of x-ray attenuation [28, 42, 43]. The former method requires a complicated detector system to produce images and remains challenged to achieve sub-millimeter range resolution.

The latter technique, where thickness measurements are correlated to variations of the proton beam intensity with depth, was used in our measurements. In order to imitate a linear slope of a depth-dose distribution in our initial measurements, a clinical field was modified to change the slope of the SOBP. The resulting depth-dose distribution, measured with a Multi-Layer Ionization Chamber [44] located at the gantry isocenter, is shown in Fig. 14. The depth dose distribution is approximately linear in the central region (ranges between 4 and 10 cm of water), although there still is a pronounced remnant of the highest energy Bragg peak at the high range end of the distribution and an almost flat low-range part, which can affect the radiographic resolution. Due to the lack of beam availability and time, no further adjustments could be made.

To calibrate the correspondence of the GEM detector signal with the RC material thickness, a right-triangular acrylic wedge of 51 mm width, 90 mm height and 150 mm maximum thickness was placed at the 10 cm detector's face (positioned at the gantry

isocenter) as shown in Fig.15a. After irradiation in a uniform scanning beam with a 200 cGy dose, the digital image was corrected for detector lateral non-uniformity. The resulting wedge image is shown in Fig. 15b. In order to obtain a signal-to-thickness calibration curve, the GEM signal was integrated along a 130 pixel (11.6 mm) wide band (also shown in Fig. 15b) and the density profile was fitted with a 3rd-order polynomial curve as a function of wedge thickness in the 28 – 99 mm range.
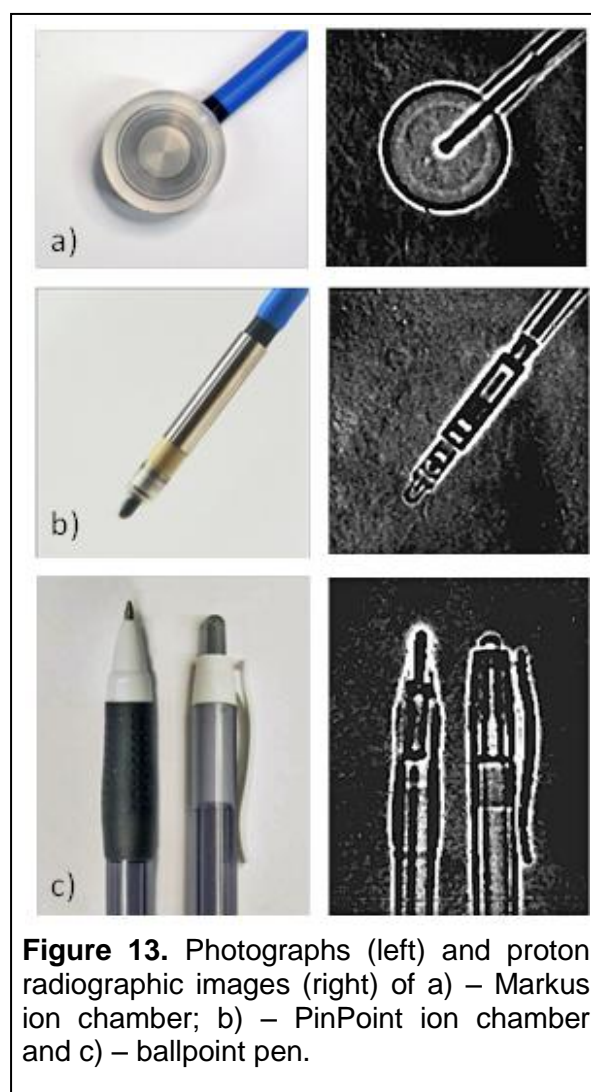

Figure 13. Photographs (left) and proton radiographic images (right) of a) – Markus ion chamber; b) – PinPoint ion chamber and c) – ballpoint pen.
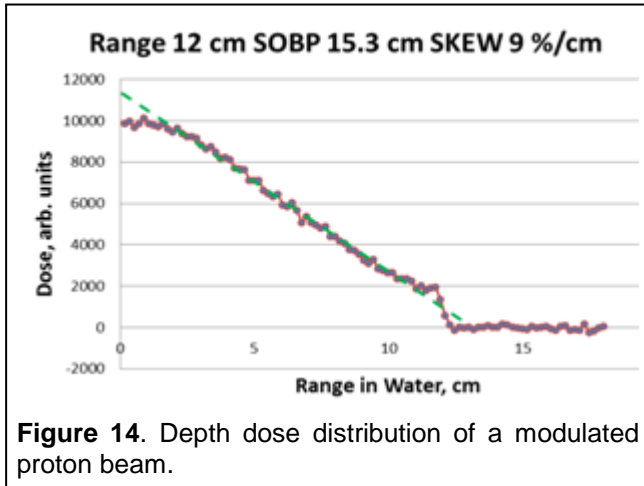
Figure 14. Depth dose distribution of a modulated proton beam.

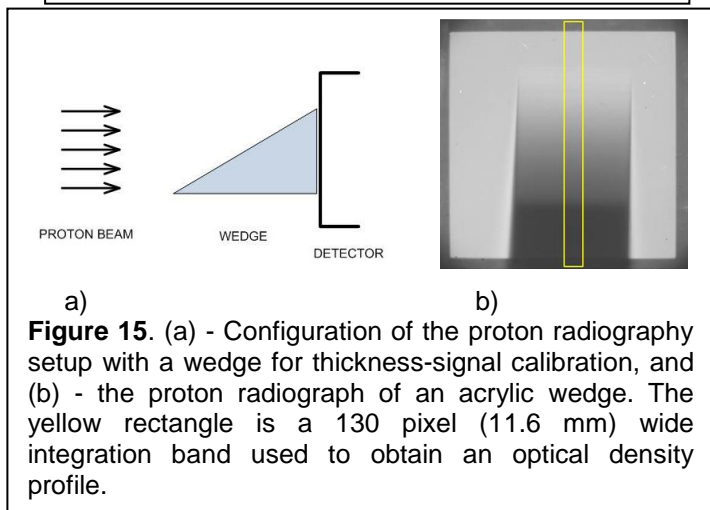a)   b)

Figure 15. (a) - Configuration of the proton radiography setup with a wedge for thickness-signal calibration, and (b) - the proton radiograph of an acrylic wedge. The yellow rectangle is a 130 pixel (11.6 mm) wide integration band used to obtain an optical density profile.

An acrylic step phantom similar in shape and material to an RC, was fabricated with several sectors consisting of steps ranging from 1.2 to 15 mm increments (Fig. 16a). This phantom was placed at the face of the detector in a similar fashion as the wedge in Fig. 15a, with one of the sectors spanning the sensitive area of the detector, and irradiated in a uniform scanning proton beam with 200 cGy dose. A radiographic image of the 5 mm step sector (after processing described below) is shown in Fig. 16b. Then the phantom was rotated by 30° and an image of another sector was taken. Acquired images were corrected for detector lateral non-uniformity, and a 7x7 pixel median filter was applied. The signal was integrated over a 100 pixel (9 mm) wide band to obtain an optical density profile which was then converted to the thickness

profile using the signal-to-thickness calibration curve. Figure 17, a profile comparison of the data obtained from radiographic images of 5 mm and 10 mm step phantom sectors, shows a good agreement except in regions near the ends of the calibration range, where the nonlinearity of the proton field depth dose distribution (Fig. 14) can affect the accuracy of signal-to-depth calibration.

4. Conclusions

The results of the studies reported above have demonstrated the feasibility of GEM detectors for dose imaging and patient-specific QA applications. However, to make it a truly clinical instrument, improvements to a full-scale OptiGEM detector are planned. Although GEM detectors of comparable area have been built before for high energy physics experiments (for example, [45]), the development of a large GEM detector for proton therapy applications presents technical challenges in increasing the reliability of operation in harsh radiation environment, reducing the discharge probability and maintaining the transverse gain uniformity on the level of the small detector. Among other improvements, this requires redesigning the GEM mounting structure to use metal instead of plastic (Rexolite) mounting frames and developing a better GEM foil stretching technique.
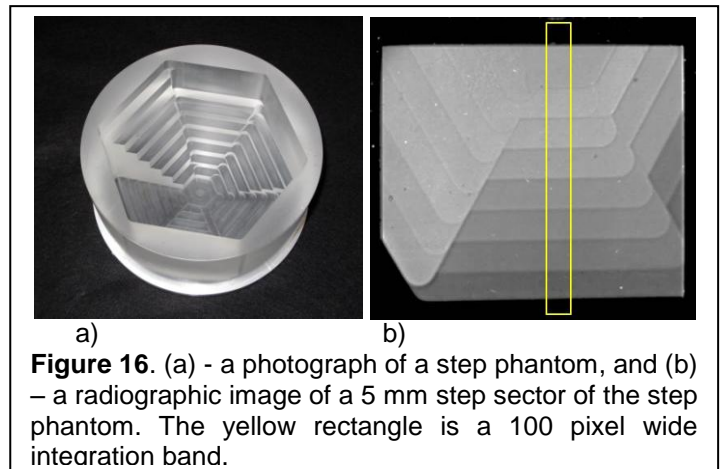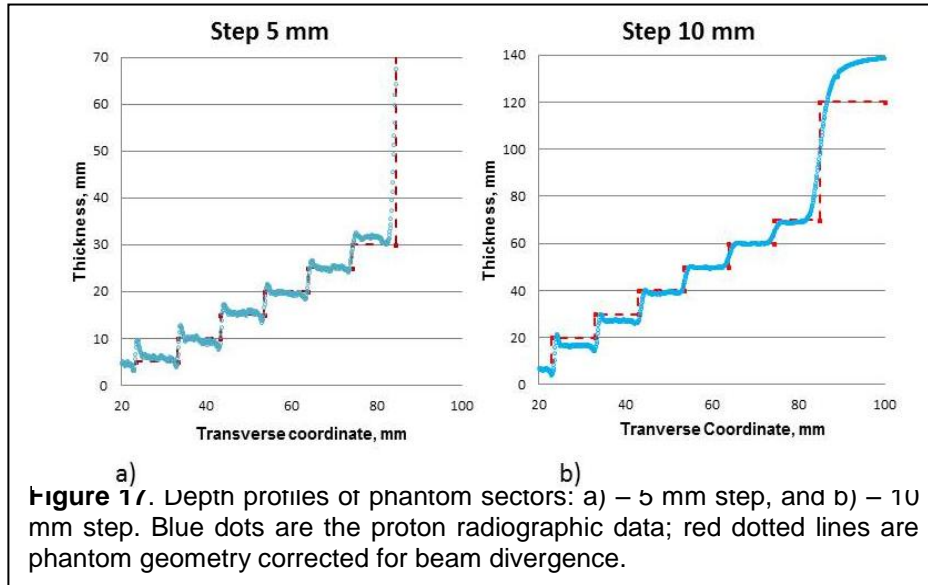

a)   b)

Figure 16. (a) - a photograph of a step phantom, and (b) – a radiographic image of a 5 mm step sector of the step phantom. The yellow rectangle is a 100 pixel wide integration band.

Figure 17. Depth profiles of phantom sectors: a) – 5 mm step, and b) – 10 mm step. Blue dots are the proton radiographic data; red dotted lines are phantom geometry corrected for beam divergence.

Further improvements may include optimization of proportions of the He/CF$_4$ gas mixture, better sealing of the detector volume and controlling the purity of gas mixture in order to improve the detector's stability of response. A moderate inconvenience of GEM detectors for clinical use is the need for gas circulation; hence, we will investigate the sensitivity of detector performance to gas impurities and the possibility of using a detector in a sealed mode.

The tests described above demonstrated the broadening of the GEM image at low isodoses somewhat diminishing the spatial resolution. The broadening is attributed to light scattering inside the GEM detector. Although the surfaces of GEM housing were black anodized in order to suppress the stray light, the anodized aluminum still retains considerable reflectivity in the visible part of the spectrum, 5 – 10% around 620 nm [46]. The light scattering inside of the detector can be significantly suppressed by applying more efficient non-reflective coating to the inside surfaces of GEM enclosure and detector's housing. Currently, there are several commercial suppliers of aluminum coating providing surfaces with total

reflectance well under 1% in the visible range. The most promising among them are the Deep Sky Black coating from Equinox Interscience [47] and Vantablack from Surrey NanoSystems [48], with the total hemispherical reflectance of 0.2 – 0.4 % in the visible part of the spectrum.

To summarize, our work on the development and characterization of innovative GEM-based detectors establish them as a very attractive tool for imaging dose distributions in the transverse plane, and as a possible dosimeter for depth dose measurements in clinical proton beams, particularly for small-field applications. For the first time, a detector developed and characterized in clinical beams has exhibited an array of properties optimized for clinical applications: sub-millimeter spatial resolution; better than 1% linearity with dose rate; linear response as a function of beam energy; high speed and easy operability. The introduction of a new He/CF$_4$ gas mixture, very close to water equivalent, helped improve the GEM detector's response in the Bragg peak region. By applying a pixel-by-pixel correction matrix, we were able to improve transverse uniformity of the detector's response, enabling it to detect dose variations on a level below 1%, far

surpassing radiochromic films in sensitivity and operability. High spatial resolution of the GEM detector is on par with scintillator screens and radiosensitive films, while the combination of high sensitivity and linearity, the absence of quenching in the Bragg peak region and the speed of data acquisition far exceed that of existing detectors. The same combination of features also makes a scintillation GEM detector a very attractive tool for high resolution proton radiography and, as our preliminary results show, for proton radiography based QA on PSDs.

Acknowledgments

References

1. de Moor, J.S., et al., *Cancer survivors in the United States: prevalence across the survivorship trajectory and implications for care.* Cancer epidemiology, biomarkers & prevention : a publication of the American Association for Cancer Research, cosponsored by the American Society of Preventive Oncology, 2013. **22**(4): p. 561-570.

2. Smith, A.R., *Vision 20/20: Proton therapy.* Medical physics, 2009. **36**(2): p. 556-568.

3. McDonald, M.W. and M.M. Fitzek, *Proton therapy.* Current problems in cancer, 2010. **34**(4): p. 257-296.

4. MEDraysintell. *Proton Therapy World Market Report Edition 2015.* 2015; http://medraysintell.com/attachments/File/MEDraysintell_Proton_Therapy_Edition_2015_-_Summary_and_Table_of_Contents.pdf

5. P.J. Kim and H.A. Shih, *The Place of Ion Beams in Clinical Applications, and references therein*, in *Ion Beam Therapy: Fundamentals, Technology, Clinical Applications*, U. Linz, Editor. 2012, Springer-Verlag: Berlin. p. 17.

6. Reinhardt, S., et al., *Comparison of Gafchromic EBT2 and EBT3 films for clinical photon and proton beams.* Medical physics, 2012. **39**(8): p. 5257-5262.

7. Boon, S.N., et al., *Performance of a fluorescent screen and CCD camera as a two-dimensional dosimetry system for dynamic treatment techniques.* Medical physics, 2000. **27**(10): p. 2198-2208.

8. *LYNX PT*. IBA Dosimetry 2015; http://www.iba-dosimetry.com/complete-solutions/radiotherapy/particle-therapy-do-simetry/lynx

9. Ramm, U., et al., *Three-dimensional BANG TM gel dosimetry in conformal carbon ion radiotherapy.* Physics in Medicine and Biology, 2000. **45**(9): p. N95.

10. Liyong, L., et al., *A novel technique for measuring the low-dose envelope of pencil-beam scanning spot profiles.* Physics in Medicine and Biology, 2013. **58**(12): p. N171.

11. Liyong, L., et al., *Experimental characterization of two-dimensional spot profiles for two proton pencil beam scanning nozzles.* Physics in Medicine and Biology, 2014. **59**(2): p. 493.

12. Arjomandy, B., et al., *Verification of patient-specific dose distributions in proton therapy using a commercial two-dimensional ion chamber array.* Medical physics, 2010. **37**(11): p. 5831-5837.

13. Arjomandy, B., et al., *Use of a two-dimensional ionization chamber array for proton therapy beam quality assurance.* Medical physics, 2008. **35**(9): p. 3889-3894.

14. Sauli, F., *GEM: A new concept for electron amplification in gas detectors.* Nucl. Instr. and Meth., 1997. **A386**(2-3): p. 531-534.

15. Fraga, F.A.F., et al., *Optical readout of GEMs.* Nucl. Instr. and Meth., 2001. **471**(1-2): p. 125-130.

16. Fraga, F.A.F., et al., *Scintillation neutron detectors with GEMs.* Intl. Workshop PSND 2001at HMI, Berlin, Germany 2001, http://www.hmi.de/bensc/psnd2001/, 2001.

17. Fraga, F.A.F., et al. *Imaging detectors based on the gas electron multiplier scintillation light*. in *Nuclear Science Symposium, 1999. Conference Record. 1999 IEEE*. 1999.

18. Timmer, J.H., et al., *A scintillating GEM for 2D-dosimetry in radiation therapy.* Nucl. Instr. and Meth., 2002. **478**(1-2): p. 98-103.

19. Fetal, S., et al., *Dose imaging in radiotherapy with an Ar-CF4 filled scintillating GEM*. Nucl. Instr. and Meth. A, 2003. **513**(1-2): p. 42-46.

20. Seravalli, E., et al., *2D dosimetry in a proton beam with a scintillating GEM detector.* Phys Med Biol., 2009. **54**(12): p. 3755-3771.

21. Klyachko, A.V., et al., *Dose Imaging Detectors for Radiotherapy Based on Gas Electron Multipliers.* Nucl. Instr. and Meth., 2011. **628**(1): p. 434-439.

22. Hoppe, R., T.L. Phillips, and M. Roach III, *Leibel and Phillips Textbook of Radiation Oncology, 3rd Edition*. 2010, Philadelphia: Elsevier/Saunders.

23. Paganetti, H., *Proton Therapy Physics*. 2012, Boca Raton, FL: CRC Press.

24. Zhao, Q., H. Wu, and I. Das. *Quality assurance of proton compensators*. in *World Congress on Medical Physics and Biomedical Engineering, IFMBE Proceedings*. 2012. Berlin, Germany: Springer.

25. Kim, J.S., et al., *Image based quality assurance of range compensator for proton beam therapy.* Korean J. Med. Phys., 2008. **19**: p. 35-41.

26. Yoon, M., et al., *Computerized tomography-based quality assurance tool for proton range compensators.* Med. Phys. , 2008. **35**: p. 3511-3517.

27. Kim, M., et al., *Development of a 3D optical scanning-based automatic quality assurance system for proton range compensators.* Medical physics, 2015. **42**(2): p. 1071-1079.

28. Park, S., et al., *Proton-radiography-based quality assurance of proton range compensator.* Physics in Medicine and Biology, 2013. **58**(18): p. 6511.

29. Park, S., et al., *Feasibility study of proton-based quality assurance of proton range compensator.* Journal of Physics: Conference Series, 2013. **444**(1): p. 012056.

30. *Gafchromic EBT3 film specifications, Ashland Inc.* 2015; http://www.ashland.com/Ashland/Static/Documents/ASI/Advanced%20Materials/gafchromic-ebt3.pdf

31. Sauli, F., *Development and applications of gas electron multiplier detectors.* Nuclear Instruments and Methods in Physics Research Section A: Accelerators, Spectrometers, Detectors and Associated Equipment, 2003. **505**(1-2): p. 195-198.

32. Nichiporov, D., L. Coutinho, and A.V. Klyachko, *Characterization of a GEM-based scintillation detector with He-CF4 gas mixture in clinical proton beams.* Phys. Med. Biol., 2015. **61**(8): p. 2972 - 2990.

33. Klyachko, A.V., *Phenix Medical OptiGEM Dose Imaging Detector User Manual*. Phenix Medical LLC internal document, 2014.

34. Klyachko, A.V., et al., *A GEM-based dose imaging detector with optical readout for proton radiotherapy.* Nuclear Instruments and Methods in Physics Research Section A: Accelerators, Spectrometers, Detectors and Associated Equipment, 2012. **694**(0): p. 271-279.

35. Tech-Etch. 2012; http://www.tech-etch.com/

36. QSI, Quantum Scientific Imaging, Inc., 12 Coteau Dr., Poplarville, MS 39470, USA 2013.

37. Fraga, M.M.F.R., et al., *The GEM scintillation in He-CF4, Ar-CF4, Ar-TEA and Xe-TEA mixtures.* Nucl. Instr. and Meth., 2003. **A 504**: p. 88-92.

38. Farr, J.B., et al., *Clinical characterization of a proton beam continuous uniform scanning system with dose layer stacking.* Medical physics, 2008. **35**(11): p. 4945-4954.

39. PTW. *PTW-Freiburg GmbH*. Lörracher Strasse 7, 79115 Freiburg, Germany. 2010; http://www.ptw.de/home_start.html

40. Schulte, R., et al., *Conceptual Design of a Proton Computed Tomography System for Applications in Proton Radiation Therapy.* Nuclear Science, IEEE Transactions on, 2004. **51**(3): p. 866-872.

41. Talamonti, C., et al., *Proton radiography for clinical applications.* Nuclear Instruments and Methods in Physics Research Section A: Accelerators, Spectrometers, Detectors and Associated Equipment, 2010. **612**(3): p. 571-575.

42. Ryu, H., et al., *Density and spatial resolutions of proton radiography using a range modulation technique.* Physics in Medicine and Biology, 2008. **53**(19): p. 5461.

43. Zygmanski, P., et al., *The measurement of proton stopping power using proton-cone-beam computed tomography.* Physics in Medicine and Biology, 2000. **45**(2): p. 511.

44. Nichiporov, D., et al., *Multichannel detectors for profile measurements in clinical proton fields.* Medical physics, 2007. **34**(7): p. 2683-2690.

45. Altunbas, C., et al., *Construction, test and commissioning of the triple-gem tracking detector for COMPASS.* Nucl. Instr. and Meth., 2002. **490**(1-2): p. 177-203.

46. Marshall J.L., W.P., Rheault J.-P., Prochaska T., Allen R. D., DePoy D.L., *Characterization of the Reflectivity of Various Black Materials.* Proc. SPIE 9147, Ground-based and Airborne Instrumentation for Astronomy V, 91474F 2014.

47. *Equinox Interscience, Pinecliffe, USA. Deep Sky Black*. 2016; http://www.eisci.com/deepsky.html

48. *Surrey NanoSystems, Newhaven, UK. Vantablack*. 2016; https://www.surreynanosystems.com/vantablack